Using cavitation to measure statistics of low-pressure events in large-Reynolds-number turbulence

A. La Porta,[a] Greg A. Voth, F. Moisy,[b] and Eberhard Bodenschatz
Laboratory of Atomic and Solid State Physics, Cornell University, Ithaca, New York 14853-2501

(Received 17 August 1999; accepted 16 February 2000)

The structure of the pressure field of a turbulent water flow between counter-rotating disks is studied using cavitation. The flow is seeded with microscopic gas bubbles and the hydrostatic pressure is reduced until large negative pressure fluctuations trigger cavitation. Cavitation is detected via light scattering from cavitating bubbles. The spatial structure of the low-pressure events are visualized using a high-speed video system. A fast photo detector is used to measure the scaling of the cavitation statistics with the pressure. This data is used to determine the shape of the tail of the probability density function for the pressure. The tail is found to be exponential and scales more rapidly with Reynolds number than the standard deviation of the pressure. This may indicate the influence of internal intermittency. © *2000 American Institute of Physics.* [S1070-6631(00)01106-5]

I. INTRODUCTION

No completely satisfactory experimental technique exists for making noninvasive measurements of the pressure field in a turbulent flow. Conventional pressure sensors are typically unable to resolve the finest scales of intense turbulence. More fundamentally, conventional sensors usually measure the pressure on the wall of the container rather than in the bulk of the flow. Pressure probes can be constructed which extend into the flow and measure the pressure at a point, but these can perturb the flow and usually suffer from velocity contamination.

In this paper, we report studies using cavitation to detect large negative pressure fluctuations in a turbulent water flow between counter-rotating disks. The large-Reynolds-number water flow is seeded with small gas bubbles and the hydrostatic pressure is adjusted so that negative pressure fluctuations go below the vapor pressure and trigger cavitation. The seed bubbles are a negligible perturbation to the system up until the moment that cavitation is triggered. The spatial and temporal resolution of the measurement is very high, and is set by the size, number density, and resonant frequencies of the seed bubbles. We use high-speed video imaging of the coherent pressure structures marked by cavitation as a way to visualize the low-pressure filaments. In addition, we study the probability distribution of large negative pressure fluctuations by measuring the light scattered from cavitating bubbles in a small region of the flow. From this we estimate the scaling with Reynolds number of the negative tail of the pressure distribution.

The importance of the pressure in the equations of fluid motion has motivated many studies of the properties of the pressure field.[1–4] Numerical simulations[5–9] and experimental measurements from conventional pressure probes[10–12] have found that the pressure distribution is skewed to negative pressures where there is an exponential tail. It has been shown analytically[13] that this does not necessarily indicate the presence of structures in the flow because even Gaussian velocity fields produce exponential pressure tails. However, a careful numerical study[7] finds that despite qualitative agreement there are significant numerical discrepancies between a pressure field derived from a Gaussian velocity field and a pressure field derived from turbulent fluid motion.

In recent years, there has also been much interest in filament-like vorticity structures in turbulent flows, and in the relationship between these structures and the negative tail of the pressure distribution. Numerical simulations at relatively low Reynolds number have found that intense vorticity regions are often tube-like structures with diameters a few times the Kolmogorov scale and lengths on the order of the largest scales in the flow.[7,14–17] Experimental investigations have used the migration of gas bubbles against the pressure gradient to visualize low-pressure filaments in turbulent water flows.[18,19] Brachet[5,6] studied the spatial distribution of vorticity and dissipation in numerical simulations and observed a link between low pressure zones and concentrated vorticity. Several other studies have been conducted to develop a more precise understanding of low-pressure structures.[10–12,20] In addition, large velocity gradients have been observed in a helium flow between counter-rotating disks at very large Reynolds number, and can be understood as signatures of Kolmogorov scale vorticity filaments.[21,22]

A central issue is the association of the observed low-pressure filaments with high-vorticity regions. In an incompressible flow the pressure is determined by the velocity field according to

$$\nabla^2 p = -\rho(e_{ij}e_{ij} - \omega_{ij}\omega_{ij}), \tag{1}$$

[a]Electronic mail: alp@max.msc.cornell.edu
[b]Present address: Laboratoroire de Physique Statistique, Ecole Normale Superieure, 24 rue Lhomond, 75231 Paris, France.

TABLE I. Turbulence parameters for the three propeller rotation rates. Re is defined as $\omega r^2/\nu$, where ω is the angular frequency, r is the radius of the propeller, and ν is the kinematic viscosity. Values are given for the Taylor scale (λ), rms velocity (u), Taylor scale Reynolds number (R_λ), and Kolmogorov scales (τ_η, η) at the center of the flow as measured in Ref. 29.

f (Hz)	Re	u (m/sec)	λ (m)	R_λ	τ_η (sec)	η (m)
7	4.40×10^5	0.78	2.12×10^{-3}	1658	6.7×10^{-4}	2.6×10^{-5}
8	5.03×10^5	0.89	1.99×10^{-3}	1772	5.4×10^{-4}	2.3×10^{-5}
9	5.65×10^5	0.99	1.89×10^{-3}	1880	4.5×10^{-4}	2.1×10^{-5}

where e_{ij} is the rate of strain tensor and ω_{ij} is the vorticity tensor.[23] From this relation it is clear that deep minima of p are associated with extended regions of excess vorticity. However, using a simple model of a filament (such as a Gaussian vorticity distribution) it can be shown that the minimum pressure is determined by the maximum azimuthal fluid velocity of the filament, not simply the peak vorticity. Therefore, the similarity hypothesis indicates that structures larger than the Kolmogorov scale typically generate the lowest pressures. This is consistent with the fact that pressure filaments are typically observed to have diameters of order of the Taylor scale, and depend very much on the nature of the flow.[20]

At the same time, cavitation in low-pressure structures has been extensively studied in the engineering community because it is a very important consideration in the design of fluid machinery.[24,25] Cavitation in this sense is very different from bubble migration visualization used in previous experiments.[18,19] In this case it is the explosive growth of seed bubbles resulting from conversion of liquid to vapor at the bubble interface. O'Hern[26] visualizes low-pressure cavitating filaments in a shear layer and connects the events to vortex structures. Interest in the effects of pressure fluctuations in cavitation led Ran and Katz[27,28] to develop a technique for nonintrusive measurements of fluctuating pressures in the bulk of a fluid by holographic bubble size measurements. They report pressure measurements in a turbulent jet and relate the low pressures to vortex rings.

The general goal of this paper is to relate the structural information about the pressure field that is obtained by visualization of cavitation with the quantitative information about the pressure distribution that is obtained by measurement of the cavitation rate as a function of pressure. In Sec. II below we describe the flow and instrumentation used in the experiments. In Sec. III we summarize the dynamics of the cavitation process and describe how cavitation can be used to characterize the pressure distribution of the flow. In Sec. IV we describe what we have learned about the structural properties of the flow and in Sec. V we describe quantitative measurements of the probability distribution function of the pressure. The results are summarized and interpreted in Sec. VI.

II. EXPERIMENTAL METHODS

A. Flow between counter-rotating disks

The experiments described in this paper were performed using a water flow in a cylindrical container driven at each end by counter-rotating disks. The container, mounted vertically, is 48.3 cm in diameter and 60.5 cm long with a planar window on one side for visualization and a small circular window at 90° for illumination. The disk-shaped propellers are open-ended cylinders 20 cm in diameter and 4.3 cm deep with 12 internally mounted radial vanes. The propellers are spaced 33 cm apart and are driven by 0.9 kW servo controlled dc motors that are coupled to the propellers with variable speed reducers. A smaller cylindrical tube surrounds each propeller, and stationary radial vanes between this inner cylinder and the outer cylinder have been installed to inhibit large-scale rotation of the flow. When the propellers are driven at their maximum rotation rate of 9 Hz, the Reynolds number (defined in Table I) reaches 5.65×10^5. Although an arbitrarily-small-Reynolds-number flow can be created, pressure fluctuations large enough to generate significant cavitation are not observed unless the propeller rotation rate is at least 7 Hz. Cavitation was measured at rotation rates of 7, 8, and 9 Hz. The Reynolds numbers and other turbulence properties for these three rotation rates are shown in Table I. The properties of this flow are described in more detail in Ref. 29.

The averaged flow produced by the propellers can be interpreted as the superposition of two basic components, a pumping mode and a shearing mode. Centrifugal pumping by the propellers produces a flow represented in Fig. 1(a). In addition, fluid near the top and bottom of the cylinder tends to rotate collectively with the propellers. Since the propellers counter-rotate, this creates a shear layer around the edge of the flow between the two propellers, as represented in Fig.

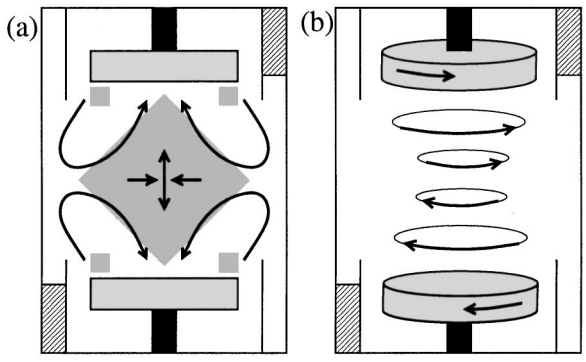

FIG. 1. Representation of the streamlines of the (a) pumping mode and (b) the shearing mode in the flow between counter-rotating disks. The shaded regions in (a) indicate parts of the flow where significant cavitation occurs.

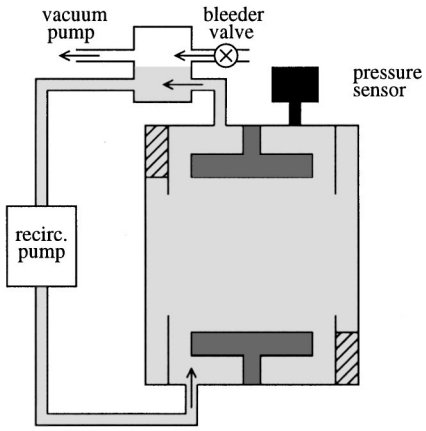

FIG. 2. Schematic diagram of the pressure control system.

1(b). Generation of vorticity in the flow is thought to result largely from the instability of this shear layer. The mean flow advects this vorticity toward the central region where it is amplified by the mean strain field [depicted by the arrows in the center of Fig. 1(a)].

In order to adjust the cavitation threshold to be within the range of pressure fluctuations in the flow, the hydrostatic pressure is controlled using the arrangement shown in Fig. 2. A recirculating loop including a small chamber is coupled to the fluid volume using flexible tubing. The chamber is mounted above the main fluid volume and the system is filled until the fluid–air interface is in this upper chamber. A water-sealed vacuum pump is used to evacuate the upper chamber and a bleeder valve open to the atmosphere is adjusted by a computer servo system to regulate the pressure in the main fluid chamber.

B. Instrumentation

Cavitation events in the flow are detected by light scattering. A small volume at the center of the flow is illuminated using a collimated light source and the light scattered at 90° is collected by imaging optics. A 400 frame per second video camera is used to record the distribution of scattering centers and detect coherent structures in the flow. The video images can be recorded with continuous illumination from a tungsten lamp, in which the camera integrates for the entire frame period, or stroboscopic illumination with a 20 μsec exposure time. The video camera is fast enough to track the evolution of large-scale structures but, as will be apparent in the discussion that follows, is too slow to resolve the dynamics of the fastest pressure events.

In order to resolve the fast dynamics and measure the statistics of cavitation events, a PIN photodiode (UDT model 455HS) was used in conjunction with the continuous light source to collect the light scattered from a 3.0 cm^3 volume at the center of the flow defined by the 1 cm depth of the illumination and approximately 2 cm diameter field of view of the detector. The photodiode was used with a transconductance amplifier with a 200 kHz bandwidth to investigate the temporal structure of the light signal. A high gain configuration having a bandwidth of 30 kHz was used to measure statistics. In the latter configuration, the noise floor in the detector was due to light scattering from seed bubbles in the flow.

The sensitivity of the detector in the high gain configuration with illumination from a tungsten lamp was measured by introducing bubbles of known size into the system and measuring the amplitude of the scattering signal. The bubbles involved are much larger than the wavelength of light, so geometrical optics is applicable and the scattering cross section scales as r^2, where r is the radius of the bubble. The detector current was found to be related to the bubble radius by $i=(3.5\times10^{-10}\,\mathrm{A/mm^2})\times r^2$. The output voltage of the transconductance amplifier in the high-gain configuration was related to the bubble radius by $\mathscr{V}=(11\,\mathrm{mV/mm^2})\times r^2$. Given that the detector noise floor is about 1 mV, a single bubble with radius 1 mm can be detected with 10:1 signal-to-noise ratio.

III. USING CAVITATION BUBBLES AS PRESSURE SENSORS

If the local pressure in a liquid goes below the vapor pressure, a vapor bubble can grow without bound by conversion of liquid to vapor at the bubble interface. However, the destabilization and dynamics of the bubble can be quite complicated due to the influence of surface tension, the thermodynamics of the vaporization process, and dynamical instabilities. There is a large and varied literature dealing with the onset and dynamics of cavitation in turbulent flows.[24–28,30] In our measurements of the pressure distribution, we will make use of a few basic properties of cavitating bubbles that can be derived from a simple model, the Rayleigh–Plesset (R-P) equation,[24] which includes viscous and inertial effects and confinement of the bubble by surface tension.

The evolution of the radius r of a spherical cavitating bubble is determined by

$$\ddot{r}=\left[\frac{1}{\rho}\left(p_i-p_\infty-\frac{2\sigma}{r}-\frac{4\mu}{r}\dot{r}\right)-\frac{3}{2}(\dot{r})^2\right]\frac{1}{r}, \tag{2}$$

where p_i is the internal pressure of the bubble, p_∞ is the external pressure field, μ is the viscosity and σ is the surface tension. We will assume that the pressure does not vary over the region into which the bubble expands, so that p_∞ is taken to be the local pressure fluctuation. For a pure vapor bubble, p_i is constant and equal to the vapor pressure p_v. In this case there is an unstable equilibrium at radius $r_0=2\sigma/(p_v-p_\infty)$. However, it is clear that pure vapor bubbles are not relevant to our experiment. They are not stable, and cavitation bubbles cannot be nucleated except from a stable seed bubble, since the pressure required to overcome surface tension diverges as the bubble radius approaches zero.

In our experiments, examination of the flow with a long working distance microscope indicates that it is seeded with bubbles of radius (35 ± 10) μm (see Sec. V D below), which have a lifetime of a minute or more. The bubbles are generated by cavitation near the propellers (indicated by the small square regions in Fig. 1) and are transported throughout the fluid volume by the strong mixing in the turbulent flow. The bubbles are eventually removed from the flow when they

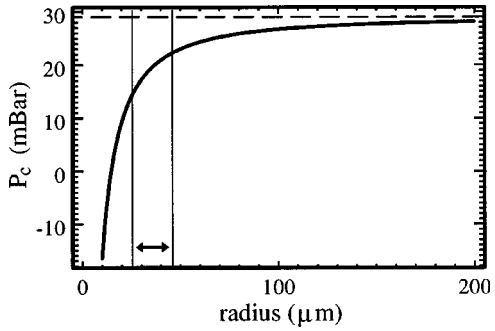

FIG. 3. The solid line is the critical pressure as a function of equilibrium bubble radius r_{eq}. The critical pressure is calculated for water using Eqs. (3) and (4) and assuming $p_0 = 100$ mbar. The dashed line is the vapor pressure, $p_v = 29$ mbar, the two vertical lines indicate the measured range of seed bubble radii.

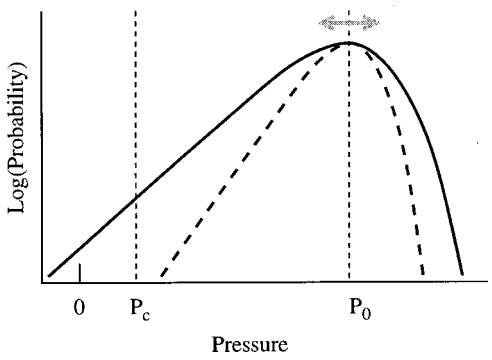

FIG. 4. Zero pressure, the cavitation threshold (p_c) and the mean pressure (p_0) in the flow are shown on an absolute scale. The probability distribution of the pressure at a point in the fluid is shown for large Reynolds number by the solid curve and for small Reynolds number by the dashed curve. The hydrostatic pressure p_0 is under experimental control (see Fig. 2).

redissolve into the fluid or coalesce into larger bubbles which float to the top of the chamber and are removed by the recirculating pump (see Fig. 2). To persist for such long times, these bubbles must be filled with a gas which is effectively insoluble in the liquid over these time scales. They are presumably created when air dissolved in the water is released into the void of the cavitating bubbles at the propellers.

The Rayleigh–Plesset equation can be applied to the gas-filled bubbles if the internal pressure is assumed to be the sum of a vapor pressure and a gas pressure, which can be approximated as an isothermal ideal gas. This gives $p_i = p_v + k/r^3$, taking $k = nRT$, where R is the gas constant, T is the constant temperature, and n is the quantity of undissolved gas in moles. A gas-filled bubble is stable as long as expansion of the bubble results in a decrease in the internal pressure that is more rapid than the decrease in surface-tension-induced confining pressure. It is found from the R-P equation that a bubble which is stable at a certain radius and pressure will restabilize at a slightly larger radius if the pressure is reduced by an infinitesimal amount. However, if the pressure goes below a certain threshold, the bubble becomes unstable and grows without bound. Ignoring inertial effects, the pressure threshold is

$$p_c = p_v - 2\left(\frac{2}{3}\right)^{3/2}\frac{\sigma^{3/2}}{k^{1/2}}. \tag{3}$$

The value of k is determined by assuming the bubble has an equilibrium radius r_{eq} at mean hydrostatic pressure p_0 and using

$$k = r_{eq}^3\left(p_v - p_0 - \frac{2\sigma}{r_{eq}}\right). \tag{4}$$

The dependence of the critical pressure p_c on the equilibrium bubble size r_{eq} at a typical value of p_0 is shown in Fig. 3. Bubbles with radius less than about 25 μm are strongly bound by surface tension, while larger bubbles become unstable at an external pressure only slightly lower than the vapor pressure. The distribution of seed bubble radii in our system is centered at 35 μm, where the critical pressure does not deviate far from the vapor pressure. We therefore expect a fairly sharp onset of cavitation when the pressure goes below the vapor pressure.

It is difficult to make an accurate estimate of the response time of the cavitation. The time required for a cavitation bubble to grow to a detectable size will depend on the detailed spatiotemporal dynamics of the pressure field, which is difficult to characterize. However, a reasonable upper bound for the bubble response speed is the resonant frequency of the seed bubbles. For the 70 μm diameter seed bubbles observed in our system, this is approximately 10 kHz.

The result we require from this analysis is that gas bubbles in our flow are stable when subject to moderate pressure fluctuations, but grow explosively when they enter a region in which the pressure is below a well-defined threshold which is slightly below the vapor pressure of the liquid. As the exploding bubbles increase in size, they become subject to the large shear in the turbulent flow and tend to be torn up into a group of smaller bubbles which is easily detected by light scattering. In effect, the seed bubbles are pressure threshold sensors, which mark regions where the pressure is below a well-defined value.

The operating principles of the technique are summarized in Fig. 4. In the turbulent flow the pressure distribution is believed to have an exponential tail at negative pressure. Cavitation is triggered whenever the pressure goes below a critical pressure p_c which is slightly below the vapor pressure, at about 20 mbar. The hydrostatic pressure p_0 is reduced until this tail crosses the critical pressure and triggers cavitation. The properties of the tail are evaluated by observing the rate and nature of cavitation events as the pressure is decreased. For this technique to be effective, the width of the pressure distribution due to turbulence must be large compared with the systematic variations in the mean pressure field in the system, mainly due to the gravitational pressure gradient. The spatial variation of the mean pressure field due to gravity is about 35 mbar, and this limits the propeller speed to be at least 7 Hz.

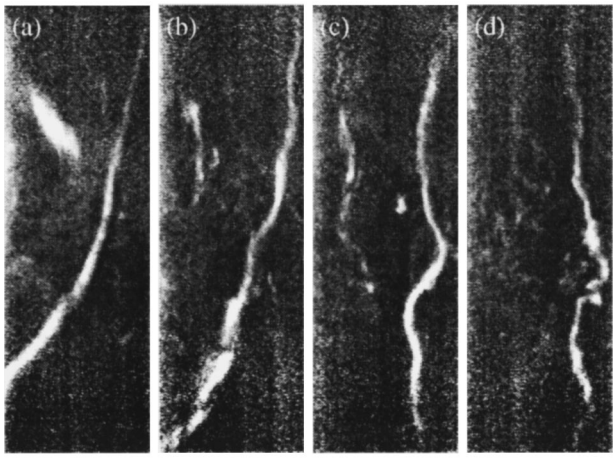

FIG. 5. Images of light scattering from cavitation and gas bubbles at pressure 70 mbar with continuous lighting. The vertical field of view is 8 cm, the propeller rotation rate is 8 Hz, and the time interval between frames is 25 msec.

IV. VISUALIZATION OF COHERENT STRUCTURES

In this section we use cavitation to visualize and study low-pressure coherent structures in the flow. The important issues are the presence and stability of low-pressure filaments, and the extent to which the anisotropy and inhomogeneity associated with the large scale influences the development of the turbulence.

Coherent structures in the flow were observed using the high-speed video system described above in Sec. II B. The large-scale properties of the flow are best visualized by setting the base pressure just above the vapor pressure. In this case, cavitation bubbles are created at a high rate throughout the fluid volume, which also results in a relatively high density of stable gas bubbles. In this regime, low-pressure structures are marked by cavitation, as well as by migration of gas bubbles towards local minima of the pressure. This is similar to the bubble migration experiments by Douady *et al.*[19] in that there does not appear to be a well-defined pressure threshold for cavitation, but local pressure minima are consistently marked by accumulations of bubbles.

Example images recorded in this regime are shown in Fig. 5. The images indicate that the large-scale flow is dominated by long vertical vortex filaments whose length can approach the largest scales of the flow. This is consistent with the vortex stretching associated with the mean strain. These structures can have lifetimes of 100 msec or more, which is of the order of the propeller overturning time. As can be seen in the sequence of images, helical undulations can appear on the long vortices, and these can lead to their destabilization.[12,18] In addition to the large vertical filaments which dominate Fig. 5, a population of smaller, more isotropically distributed vortex filaments is also present.

The images have a different character when the pressure is set higher, where stronger negative pressure fluctuations are required to nucleate cavitation. (This corresponds to p_0 being moved further to the right as shown in Fig. 4.) In this case, cavitation is infrequent and consists of brief flashes of light scattering. These flashes consist of a group of small bubbles, which persists for the duration of the pressure fluctuation (typically a few milliseconds) and then disappears. These cavitation events appear to be triggered when the local pressure goes below a well-defined threshold.

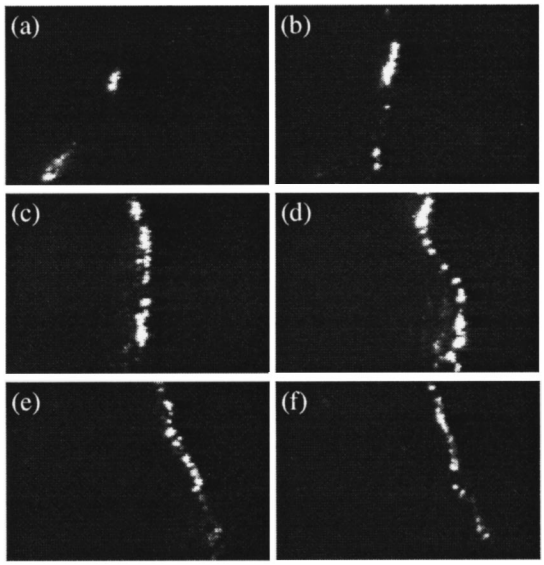

FIG. 6. Images of light scattering from cavitation nucleated by a vertical filament. The pressure is 120 mbar, the propeller rotation rate is 8 Hz, the horizontal field of view is 3 cm, and the time interval between frames in 7.5 msec. The images were taken with stroboscopic lighting.

The rare cavitation events observed at higher pressures are typically much more compact in space and time than the long filaments observed at low pressure, and usually occur in the diamond-shaped region indicated in Fig. 1. Figure 6 shows a large, long-lived cavitation event observed in the center of the flow at a relatively high pressure of 120 mbar. The event lasts for about 40 msec, and consists of a ''necklace'' of cavitation bubbles, evidently marking a filament of strong vorticity. Although this example is one of the larger and longer lived filaments observed in this pressure regime, it is much smaller than the integral scale filaments observed at low pressure.

The vertical filaments observed at the center of the flow are sometimes observed to cluster in braid-like structures such as the event shown in Fig. 7. In such configurations, the filaments are mutually advected, causing them to orbit each other, sometimes resulting in the formation of a helical con-

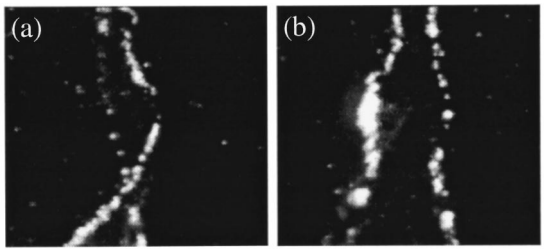

FIG. 7. Images of light scattering from cavitation nucleated by a pair of braided vertical filaments. The pressure is 135 mbar, the propeller rotation rate is 8 Hz, and the field of view is 1.9×1.9 cm. The images were made with stroboscopic lighting and the time interval between the two frames is 5 msec.

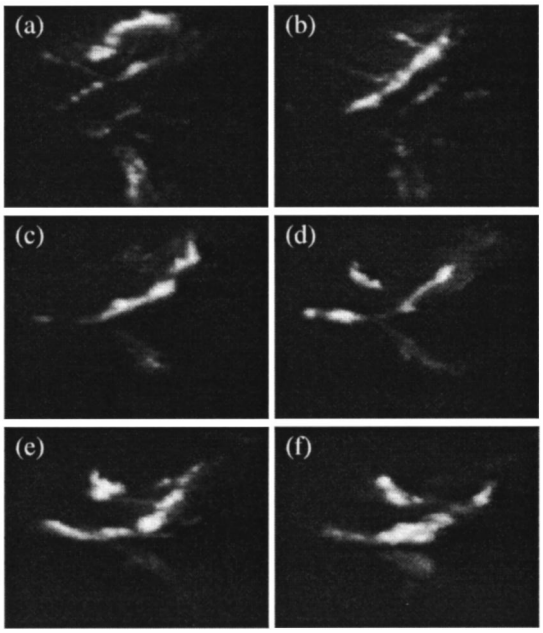

FIG. 8. Images of light scattering from cavitation nucleated by a horizontal filament. The pressure is 120 mbar, the propeller rotation rate is 8 Hz, the magnification is similar to Fig. 6, and the view is horizontally displaced 3 cm from the center of the flow. The time interval between frames in 7.5 msec, and the images were taken with continuous lighting.

figuration. When observing such structures, it is important to use stroboscopic lighting (as was used in Fig. 7). Under continuous lighting bubbles caught in the peripheral velocity field of a vortex can trace out helical trajectories and give the appearance of a braid of vortices.

Figure 8 shows an example of a long-lived cavitation event observed off the center of the flow, in the region where there is strong shear between the counter-rotating fluid above and below the mid-plane of the fluid chamber. Horizontally oriented vortex filaments can be observed, apparently arising from the Kelvin–Helmholtz instability of the shear layer. More disorganized flame-like cavitation events are also observed in this region of the flow.

Some general conclusions can be drawn from the imaging study. The images support a model in which vortices are formed in the shear layer, then are advected to the central region of the flow where they are amplified by the mean strain. The large scales of the flow are dominated by long vertical filaments up to 10 cm in length (Fig. 5), but the deepest negative pressure fluctuations resemble filaments but rarely exceed a few centimeters in length (Figs. 6 and 8). The large vortex filaments observed at low hydrostatic pressure (Fig. 5) and the smaller filaments observed at higher pressure (Fig. 6) both exhibit a tendency to align with the vertical axis. This suggests that the small, intense filaments result from local amplification of the large weaker filaments, although there is no direct evidence of this. Compared with the work of Cadot *et al.*,[12] filaments in the center of our flow exhibit a greater tendency to be aligned with the mean strain. In Cadot's experiment, filaments were more often horizontal and appeared to be bound to the wall. This may be because the geometry of our flow results in a greater pumping efficiency [see Fig. 1(a)] relative to the shearing and wall interactions.

Another issue is whether the low-pressure filaments, such as the one shown in Fig. 6, can be identified with the Kolmogorov scale vorticity filaments, or ''worms,'' which have been found in direct numerical simulation of moderate Reynolds number turbulence.[7,14–17] Such structures are also thought to account for regions of large velocity gradient observed in large-Reynolds-number turbulence in helium gas.[21] The apparent diameter of the vortex core in Fig. 6 and in other similar examples is estimated to be about 1 mm. This is of the order of the Taylor microscale, and 50 times larger than the Kolmogorov scale. The observed low-pressure events do not appear to be worms. However, Kolmogorov-size filaments would be very difficult to observe by cavitation, since these events are not expected to produce pressure fluctuations as deep as those produced by the larger structures.[7]

V. STATISTICS OF CAVITATION EVENTS

In the previous section, the spatial distribution of cavitation has been used to visualize the large coherent structures in the turbulent flow. In this section, we will attempt to extract quantitative information about the probability density function (PDF) for the pressure. For this, the photodiode detector described in Sec. II B was used to measure time series of the scattering intensity from a 3 cm^3 region at the center of the flow.

The relationship between the scattering intensity signal and the video images is evident from Fig. 9. The images show light scattering at the center of the flow and the graph shows the photodiode current and integrated video intensity during the same time interval. Increased activity is measured in the photodiode signal when a coherent structure is observed in the video sequence. However, the inset indicates that the dynamics of the photodiode signal is much faster than the frame rate of the camera. Close examination indicates the photodiode signal consists of clusters of 50–100 μsec spikes. (Runs taken with higher temporal resolution reveal that spikes as narrow as 10 μsec can occur.) This time scale is shorter than what one would expect from the explosion and collapse of an individual cavitating bubble, as estimated based on the Rayleigh–Plesset model. In the course of calibration runs, we have observed similar spiking associated with the vibration of stable gas bubbles. We therefore attribute these fast fluctuations in scattering to random deformations of the cavitation bubbles when they are subject to the fluctuating strain of the turbulent flow. In effect, vibrating bubbles sparkle.

As discussed in Sec. III above, the basic idea behind our measurement of the pressure statistics is that the small gas bubbles which are distributed throughout the flow act as pressure threshold sensors. They are stable at the mean pressure but explode when they enter a region where the pressure is below a certain threshold. The resulting spray of small bubbles is detected by the optical intensity detector. Our strategy is to find the functional dependence of the level of cavitation activity on the applied mean hydrostatic pressure

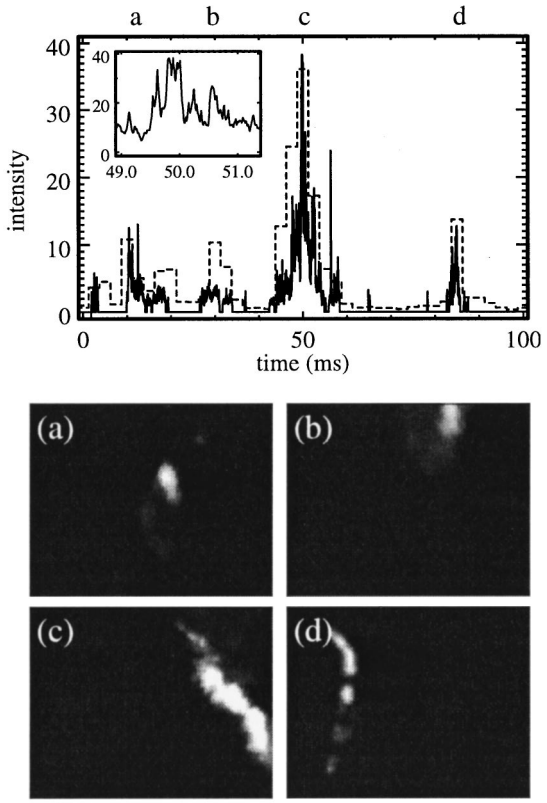

FIG. 9. The graph shows the time series of scattering intensity for a typical event at propeller rotation rate 8 Hz and at a pressure of 120 mbar with continuous lighting. The solid line indicates the photodiode current and the dashed line indicates the integrated intensity from the video camera. The inset graph shows a detail of the photodiode signal over a time period equal to the camera integration time. The four images show the light scattering measured by the camera at times (a) 10 msec, (b) 30 msec, (c) 50 msec, and (d) 85 msec, as indicated by the lower case letters set above the graph. The field of view for the images is 2.5 cm×2.0 cm^2 and the depth of illumination is 1 cm. The measurement volume for the photodiode is defined in Sec II B.

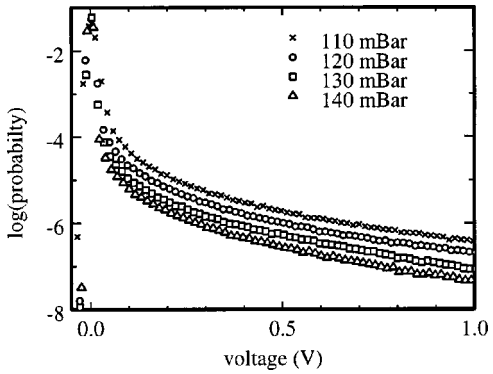

FIG. 10. Probability distribution of the intensity detector output at propeller speed 8 Hz. The voltage is related to the photocurrent by $V=(10\,\mathrm{M}\Omega)i_p$. The distributions were accumulated after approximately 60 min of continuous acquisition at 100 kHz.

p_0 and relate this to the pressure distribution. By performing this analysis at several values of the Reynolds number we can investigate the scaling of pressure statistics. However, there is more than one statistical quantity that can be used to measure the level of cavitation activity, and the challenge is in determining which of these is most easily related to the pressure PDF, and is least likely to be biased by systematic or random errors.

A. Cavitation on-fraction

The most straightforward measure of cavitation activity is the fraction of the time that cavitation is occurring in the 3 cm^3 measurement volume (defined in Sec. II B), which we will call the *cavitation on-fraction*. This quantity can be obtained by measuring the fraction of the time that a light scattering signal is detected in the measurement volume. Figure 10 shows the probability distribution of the measured scattering intensity for a propeller speed of 8 Hz. The peak near zero intensity is slightly shifted and broadened due to the light scattering from the seed bubbles. The long, nominally exponential tail for positive intensity is due to the cavitation signal. The cavitation on-fraction is obtained by integrating this probability distribution from a small voltage threshold to the limit of the ADC at 2.0 V. To maximally discriminate between the zero peak and the cavitation signal, the lower limit is taken to be 0.1 V, but the results are not changed if the value is further increased.

The cavitation on-fraction is closely related to the probability distribution of the pressure. Returning to Fig. 4, the solid and dashed curves represent the pressure distribution on a logarithmic scale. They are drawn to reflect the accepted form of the pressure distribution in a turbulent flow; Gaussian for small pressures but with an exponential tail for negative pressure fluctuations.[1–4] The fraction of time that cavitation occurs at a point in the flow is expected to be proportional to the integral of this curve over the pressure interval $(-\infty,p_c)$, i.e., the cumulative distribution function (CDF) of the pressure. The cavitation on-fraction for our measurement volume would be equal to the CDF multiplied by a constant spatial factor. This spatial factor is related to the number of pressure coherence volumes contained in the measurement volume. As will be shown below, the cavitation on-fraction (and therefore the CDF) is found to be exponential with pressure. This implies that the PDF is also exponential with the same pressure decay constant.

The precise relationship between the cavitation on-fraction and the pressure CDF will be influenced by several factors. The flow may be perturbed by the cavitation itself, and the pressure threshold is slightly blurred due to imperfect discrimination and due to the distribution of seed bubble sizes. However, in the case where the CDF is exponential and the pressure distribution is self-similar, these factors are independent of pressure and should cancel out when we consider the scaling of cavitation rate with pressure.

The upper panel of Fig. 11 shows the cavitation on-fraction as a function of pressure at three different Reynolds numbers. The curves indicate that the cavitation rate scales exponentially with the pressure. The lower panel of Fig. 11 shows the same data on a log scale, along with least-square linear regressions. We conclude that the PDF of pressure is of the form $P(p)=\exp[-(p-p_0)/\alpha]$ with pressure constants $\alpha=26.6$, 35.4, and 48.1 mbar for propeller speeds of 7, 8, and 9 Hz, respectively. These pressure constants varied by only a few percent when the threshold was varied between

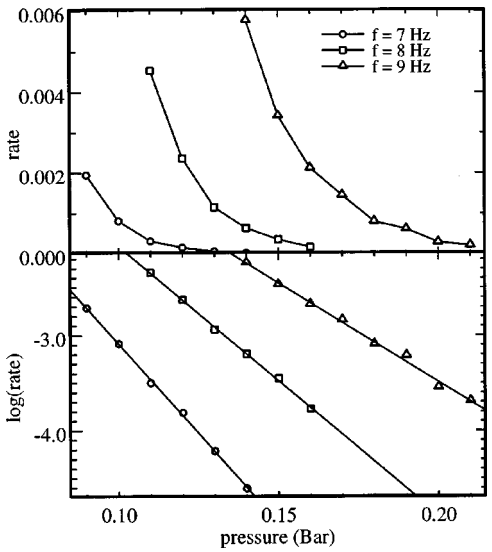

FIG. 11. The top panel shows the integral of the intensity probability distribution from 0.1 V to the saturation value. Data is shown as a function of pressure for three different values of the Reynolds number. The bottom panel shows the same data on a log scale.

0.1 and 0.2 V, or when number of seed bubbles was increased by using a 0.272 mol/L NaCl solution in place of pure water.

This result indicates that the negative tail of the pressure distribution is, in fact, exponential. As mentioned above, since the pressure distribution is found to be self-similar, any corrections to the cavitation signal resulting from spatial factors, imprecise discrimination of cavitation or perturbations to the flow by cavitation events should be independent of pressure, and should not affect the value of the pressure constant.

B. Event rate

It would be of interest to use a measure of activity which is less dependent on how the pressure fluctuation continues to develop after cavitation has been triggered. An alternative is to measure *how often* the pressure goes below the cavitation threshold. In this case, the time interval between rare cavitation events would be long enough to insure that the flow has effectively forgotten the previous cavitation event when a new event occurs. Although we regard this event rate as potentially cleaner than the cavitation on-fraction, it is not as easily related to the pressure CDF as the cavitation on-fraction. To relate the event rate to the pressure CDF we must have information about the duration of the pressure events.

In order to measure the cavitation event rate, the cavitation time series was analyzed in terms of *pulses* and *bursts* of cavitation. A pulse is considered to have occurred whenever the scattering signal goes above a certain threshold, set significantly above the detector noise level. When a pulse is detected, it is delimited by scanning forward and backward in time to the point where the signal goes below a second, lower threshold that is set just above the noise level. A pulse

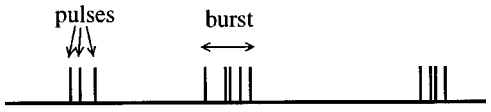

FIG. 12. Pulses and bursts in the time series of the scattered intensity signal.

typically results from the explosion and disappearance of a single cavitation bubble. It is evident that the pulses are normally not independent events. It can be seen in Fig. 9 that numerous cavitation pulses may be produced by a single long-lived pressure structure.

To measure the true event rate, it is necessary to group the individual pulses into bursts of cavitation activity. The temporal structure of the scattered intensity signal, illustrated in Fig. 12, can be characterized by measuring the wait time between consecutive pulses. The distribution of wait times between pulses for data taken at 8 Hz is shown in Fig. 13. The distribution has a sharp peak for times of 0.1 ms or less, indicating highly correlated pulse events within a burst. However, the distributions all exhibit exponential tails that appear linear on the semi-log plot. The exponential distribution of wait times is characteristic of the Poisson statistics of uncorrelated events, which we associate with the interburst wait time. By measuring this time constant, we are separating out the rate of uncorrelated cavitation bursts from the correlated pulses which occur within a burst.

The scaling of this uncorrelated event rate with pressure is shown for three values of the Reynolds number in Fig. 14. Again, the level of activity scales exponentially with pressure. (A noticeable deviation from an exponential function is observed in the data at 7 Hz, which has a low event rate. This may be due to pickup of intermittant electrical pulses emitted by the dc motors that drive the propellers.) The pressure constants obtained are $\alpha=27.0$, 44.1, and 68.5 mbar for data at 7, 8, and 9 Hz, respectively. Again, α increases with propeller speed, indicating that the pressure tail increases with Reynolds number. However, the scaling with Reynolds number is more rapid for the event rate than for the cavitation on-fraction. This is expected because the characteristic time

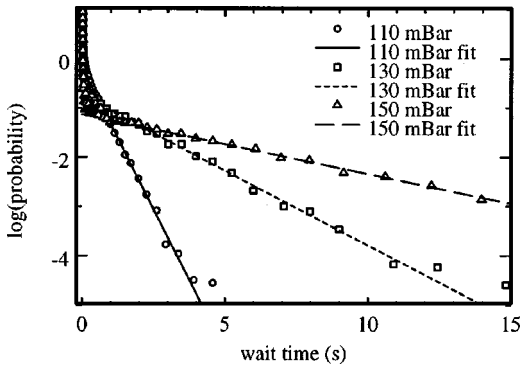

FIG. 13. The distribution of wait times for three different values of the pressure at 8 Hz is represented by the symbols. The distribution is compiled with a variable absolute bin width, but a constant relative bin width of 15%. The lines indicate least-square linear fit to the tails of the distributions.

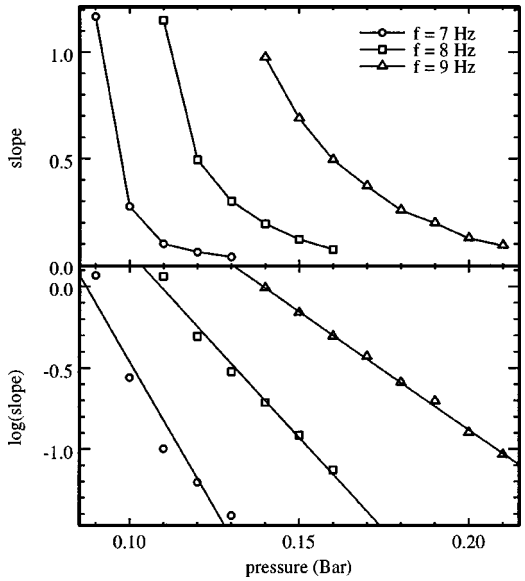

FIG. 14. The scaling of the uncorrelated event rate with pressure for three values of the propeller speed. The upper graph shows the event rate on a linear scale. The lower graph shows the event rate on a log scale, with least-squares linear regression indicated by the solid lines.

scales for pressure fluctuations become shorter as Reynolds number increases.

C. Burst length

Another quantity of interest is the mean burst length. The wait-time analysis presented in Sec. V B does not yield a value for the burst length, but this quantity can be roughly estimated from the autocorrelation function of the intensity signal. The log of the autocorrelation function is shown for several values of the pressure at 8 Hz in Fig. 15. The autocorrelation is monotonically decreasing, so a practical measure of the correlation time is the integral time scale, shown in Fig. 16. For all three values of the Reynolds number the burst time are seen to increase from 2 msec to about 8 msec as the pressure is decreased. The effect is rather weak, since the burst length increases by a factor of 4 over the same range of pressure for which the cavitation on-fraction increases by a factor of nearly 100.

The order of magnitude of the burst duration can be used to evaluate the robustness of our measurements. The mean

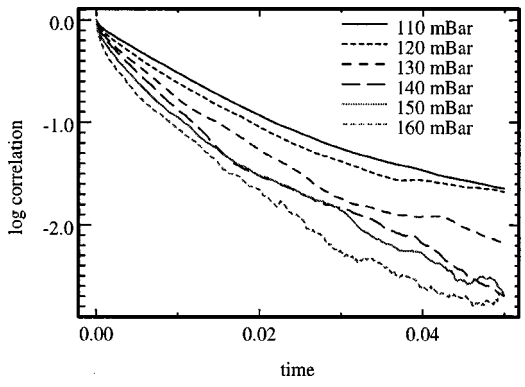

FIG. 15. Autocorrelation function of pulses at 9 Hz.

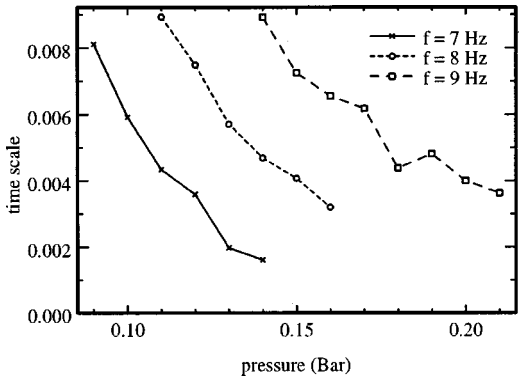

FIG. 16. Integral time scale of autocorrelation as a function of pressure at three values of the Reynolds number.

fluctuating velocity in the flow is about 0.5 m/sec and the field of view is approximately 2.0 cm, giving a sweeping time of approximately 40 msec. The fact that the bursts are significantly shorter than this indicates that the dynamics we observe are due to the lifetimes of the structures rather than the sweeping of stable structures through our field of view. In addition, the burst duration is short compared with the uncorrelated event rate, and both of these are small compared with the overturning time of the largest scales in the flow. This indicates that the flow has lost its memory of the previous cavitation event when a new event begins.

D. Systematic effects due to variation in seed bubble density

The major difficulty in the interpretation of the statistical results is the seed bubbles for the bulk cavitation are generated by cavitation on the propellers. The density of seed bubbles therefore depends on the pressure and Reynolds number.

The distribution of sizes of the seed bubbles was determined by measuring the separation of the front and rear surface reflections from seed bubbles using a large working distance microscope. The mean bubble radius was found to be approximately 35 μm, with a standard deviation of about 10 μm. As the propeller speed was increased from 7 to 9 Hz, the mean bubble size decreased by an amount small compared with its standard deviation. More importantly, the distribution of bubble sizes had no appreciable dependence on the pressure. Since our results only depend on the scaling of the cavitation process with pressure and not on the absolute cavitation rate, we are only sensitive to the pressure dependence.

The number density and homogeneity of the seed bubbles was determined by measuring the dc output level of the scattered intensity detector. The number density of the bubbles does depend on the pressure. Figure 17 shows the scaling of this dc scattering level with pressure and Reynolds number. The scaling of the bubble seeding is roughly exponential, giving pressure constants of α=45.6, 51.8, and 68.9 mbar at 7, 8, and 9 Hz, respectively.

The variation in seed bubble density is a serious concern. At lower seed densities there is a greater probability that a

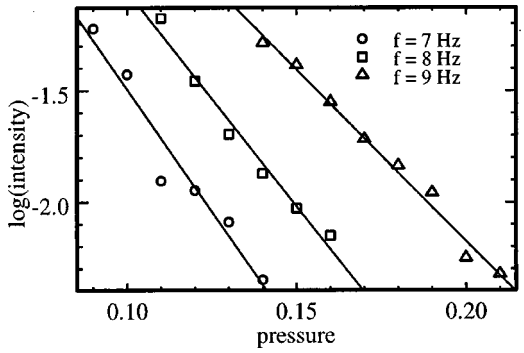

FIG. 17. Background scattering intensity. The exponential pressure constants are α=45.62, 51.8, and 68.9 mbar are 7, 8, and 9 Hz, respectively.

low pressure event will be missed because it is unseeded. The seed density variation in our system would therefore tend to augment the increase in cavitation activity that occurs as the pressure is lowered. However, the sensitivity of our statistics to the seed bubble density is mitigated by the fact that we operate in a regime where the effect of the seeding appears to be saturated.

In the cavitation on-fraction, we must assume that each pressure event is continuously marked by cavitation. Visual inspection of the data (see Figs. 6, 8 and 9) indicates that this threshold is met. To confirm this, the run at 9 Hz propeller speed was repeated with a 0.27 mol/L NaCl solution instead of water, which has the effect of increasing the number density of seed bubbles by a factor of 2 while preserving the seed bubble size. The measured pressure constant was the same to within a few percent, strongly suggesting that we are in a regime where the measurements are not sensitive to the seed density.

In the event rate data, the condition is that each pressure fluctuation is marked by at least one cavitation pulse. The wait time distributions indicate that there are, on average, significantly more than one cavitation pulse per burst. The probability that a pressure event will be unmarked appears to be small, even at the lower bubble seed densities. The lower seed density should deplete the large peak at zero time delay, without changing the uncorrelated tail of the wait time distribution. Despite this, the run with the 0.27 mol/L NaCl solution resulted in a 20% increase in the wait time pressure constant, suggesting that this statistic is more sensitive to seeding density than the cavitation on-fraction.

Despite the fact that our results do not appear to be strongly dependent on the seed bubble density, it would be advantageous to move away from a self-seeding system to one in which the seed bubbles are introduced into the flow under experimental control. This would allow the density to be held constant, which would simplify the interpretation of the data.

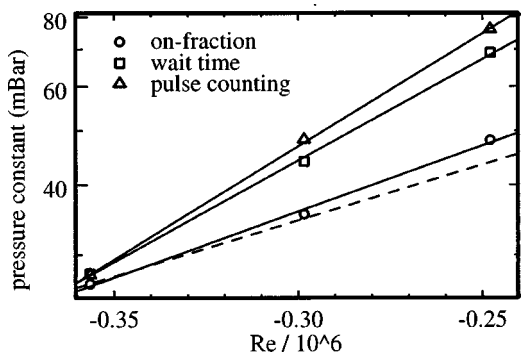

FIG. 18. Scaling of the pressure constant with Re, on a log–log plot. The pressure constants are derived from the intensity distribution (Fig. 11), the uncorrelated burst rate (Fig. 14), and from simple counting of the number of pulses per unit time. Straight line fits indicate scaling with Re^{γ} with γ of 2.36, 3.63, and 4.04 for the intensity, wait time and pulse counting methods, respectively. The dashed line indicates the expected Re^2 scaling.

E. Discussion of statistical results

In this section we have discussed two fundamentally different measures of cavitation activity; the cavitation on-fraction measures *how much* cavitation occurs and the burst rate measures *how often* cavitation occurs in a small volume of the flow. The cavitation on-fraction is thought to be closely related to the pressure PDF. The burst rate is a well-defined statistic, but is not easily related to the pressure PDF and has not been extensively studied in the literature.

The measurement of the pressure constants in Fig. 11 may be compared with results of direct numerical simulation (DNS) of turbulence. The comparison requires the pressure data to be scaled by the pressure variance in our flow, which is difficult to measure. Using an estimated value of the pressure variance, the numerical values obtained in Fig. 11 are a factor of 2 larger than DNS results reported by Vedula and Yeung[8] and by Pumir.[7] This disparity may well be due to the mean strain imposed on our flow by the pumping action of the propellers [see Fig. 1(a)], which appears to be a significant influence on the low-pressure structures.

Another important issue is the scaling of the pressure tail with the Reynolds number. In Fig. 18 the pressure constants obtained from three different cavitation statistics are plotted as a function of Reynolds number and compared with the expected $(Re)^2$ scaling. These are the on-fraction and wait time discussed earlier, plus a third derived from simple counting of pulses. The range of Reynolds number accessible is too small to provide a strong test of the scaling. However, a linear fit to the log–log plot indicates that the scaling of the pressure constants of all three quantities is faster than the expected $(Re)^2$. The cavitation on-fraction, which is more or less directly related to the pressure PDF, scales as $(Re)^{2.3}$, suggesting the pressure tail grows slightly faster than the rms pressure. The deviation of the exponent from the expected value may be interpreted as an intermittency correction. This effect has been explored in numerical simulations,[7,8] but direct comparison with our work is difficult because the simulations are at much lower Reynolds number. We cannot definitively conclude that the deviation from the expected scaling is due to intermittency because of the relatively narrow scaling range and because of possible biases resulting from variations in the seeding density. The burst and pulse event rates do scale significantly faster than $(Re)^2$, although the predicted scaling for these quantities is unclear.

VI. CONCLUSIONS

This study allows us to draw several important conclusions about large-Reynolds-number turbulence between counter-rotating disks. Visualization of the flow using cavitation at low hydrostatic pressure (near the vapor pressure) gives results similar to bubble migration experiments which were performed by Hopfinger *et al.* and by Douady *et al.*[18,19] Pressure minima are marked by cavitation and by migration of gas bubbles. The large-scale structure of the pressure field is dominated by vortex filaments with core diameters of the order of a millimeter, which is consistent with the Taylor scale in the range of Reynolds number we have studied. The length of the filaments can approach the largest scale of the flow.

The cavitation at higher hydrostatic pressure (further above the vapor pressure) gives more quantitative information about the pressure field. It highlights regions in which a deep pressure minimum has gone below a well-defined threshold (the vapor pressure with a small correction due to surface tension). Compared with those observed at low hydrostatic pressure, these structures are more intense and more compact in space and time, as indicated by the images (Figs. 6–8) and the burst length measurement (Fig. 16). The core diameter of these short, intense filaments also appears to be of the order of the Taylor microscale, but their length is typically just a few centimeters. The fact that the long filaments at low hydrostatic pressure and the shorter filaments observed at higher hydrostatic pressure both tend to be vertically oriented suggests that they are associated with each other, and that the small strong filaments result from local amplification of the larger ones.

The filaments appear to be too large to correspond to the Kolmogorov scale events (worms) which have been investigated in simulations and experiments.[7,14–17,21] However, the worms are not expected to produce pressure fluctuations that are as strong as the larger filaments[7] and probably would not trigger cavitation. The fact that the observed pressure structures tend to be aligned with the mean strain indicates that they are significantly influenced by the large-scale features of the flow between counter-rotating disks, even at very high Reynolds number.

The most important result is the statistical characterization of cavitation as a function of pressure and Reynolds number. It is found that there is no well-defined cavitation inception point, but that there is an exponential increase of cavitation activity as the hydrostatic pressure is decreased, effectively bringing the critical pressure closer to the mean hydrostatic pressure. We have made an argument that the exponential increase in cavitation activity reflects the exponential tail of the pressure PDF of the turbulent flow. The exponential pressure constant of the cavitation on-fraction is expected to be a direct measure of the exponential tail of the pressure PDF. Despite the complication introduced by the dependence of the seed bubble density on pressure, we have found that cavitation can be a precise tool for noninvasively characterizing the pressure distribution in a high-Reynolds-number turbulent flow. Our measurements confirm the expected exponential tail of the pressure PDF, and are consistent with DNS simulations of isotropic turbulence. The pressure tails scale more rapidly with Reynolds number than the rms pressure, and this may be evidence of internal intermittency.

ACKNOWLEDGMENTS

We would like to thank Bernard Yurke and Lucent Technologies Bell Labs Innovations for providing the high-speed video system used in this experiment. We also thank Eric D. Siggia and Patrick Tabeling for useful discussions. This research is sponsored by the National Science Foundation under Grant No. PHY-9722128.

[1] G. K. Batchelor, ''Pressure fluctuations in isotropic turbulence,'' Proc. Cambridge Philos. Soc. **47**, 359 (1950).
[2] R. H. Kraichnan, ''Pressure field within homogeneous aniosotropic turbulence,'' J. Acoust. Soc. Am. **28**, 65 (1956).
[3] W. W. Willmarth, ''Pressure fluctuations beneath turbulent boundary layers,'' Annu. Rev. Fluid Mech. **7**, 13 (1975).
[4] W. K. George, P. D. Beuther, and R. E. A. Arndt, ''Pressure spectra in turbulent free shear flows,'' J. Fluid Mech. **148**, 155 (1984).
[5] M. E. Brachet, ''The geometry of small-scale structures of the Taylor-Green vortex,'' C. R. Acad. Sci. Paris, Ser. II **311**, 755 (1990).
[6] M. E. Brachet, ''Direct simulation of three-dimensional turbulence in the Taylor-Green vortex,'' Fluid Dyn. Res. **8**, 1 (1991).
[7] A. Pumir, ''A numerical study of pressure fluctuations in three-dimensional, incompressible, homogeneous, isotropic, turbulence,'' Phys. Fluids **7**, 630 (1994).
[8] P. Vedula and P. K. Yeung, ''Similarity scaling of acceleration and pressure statistics in numerical simulations of isotropic turbulence,'' Phys. Fluids **11**, 1208 (1999).
[9] N. Cao, S. Chen, and G. D. Doolen, ''Statistics and structures of pressure in isotropic turbulence,'' Phys. Fluids **11**, 2235 (1999).
[10] S. Fauve, C. Laroche, and B. Castaing, ''Pressure fluctuations in swirling turbulent flows,'' J. Phys. II **3**, 271 (1993).
[11] P. Abry, S. Fauve, P. Flandrin, and C. Laroche, ''Analysis of pressure fluctuations in swirling turbulent flows,'' J. Phys. II **4**, 725 (1994).
[12] O. Cadot, S. Douady, and Y. Couder, ''Characterization of the low pressure filaments in a three-dimensional turbulent shear flow,'' Phys. Fluids **7**, 630 (1995).
[13] M. Holzer and E. D. Siggia, ''Skewed, exponential pressure distributions from Gaussian velocities,'' Phys. Fluids **5**, 2525 (1993).
[14] E. D. Siggia, ''Numerical study of small-scale intermittency in three-dimensional turbulence,'' J. Fluid Mech. **107**, 375 (1981).
[15] A. Vincent and M. Meneguzzi, ''The spatial structure and statistical properties of homogeneous turbulence,'' J. Fluid Mech. **225**, 1 (1991).
[16] J. Jimenez, A. Wray, P. Saffman, and R. Rogallo, ''The structure of intense vorticity in isotropic turbulence,'' J. Fluid Mech. **255**, 65 (1993).
[17] J. Jimenez and A. A. Wray, ''On the characteristics of vortex filaments in isotropic turbulence,'' J. Fluid Mech. **373**, 255 (1998).
[18] E. J. Hopfinger, F. K. Browand, and Y. Gagne, ''Turbulence and waves in a rotating tank,'' J. Fluid Mech. **125**, 505 (1982).
[19] S. Douady, Y. Couder, and M. E. Brachet, ''Direct observation of the intermittency of intense vorticity filaments,'' Phys. Rev. Lett. **67**, 983 (1991).
[20] E. Villermaux, B. Sixou, and Y. Gagne, ''Intense vortical structures in grid-generated turbulence,'' Phys. Fluids **7**, 2008 (1995).
[21] F. Belin, P. Maurer, P. Tabeling, and H. Willaime, ''Observations of intense filaments in fully developed turbulence,'' J. Phys. II **6**, 573 (1996).
[22] H. Willaime, F. Belin, and P. Tabeling, ''Structures and transition in a high Reynolds number experiment,'' Eur. J. Mech. B/Fluids **17**, 489 (1998).
[23] G. K. Batchelor, *An Introduction to Fluid Dynamics* (Cambridge U. P., Cambridge, 1967).
[24] M. S. Plesset and A. Prosperetti, ''Bubble dynamics and cavitation,'' Annu. Rev. Fluid Mech. **9**, 145 (1977).
[25] R. E. A. Arndt, ''Cavitation in fluid machinery and hydrolic structures,'' Annu. Rev. Fluid Mech. **13**, 273 (1981).
[26] T. J. O'Hern, ''An experimental investigation of turbulent shear flow cavitation,'' J. Fluid Mech. **215**, 365 (1990).

[27]B. Ran and J. Katz, ''The response of microscopic bubbles to sudden changes in the ambient pressure,'' J. Fluid Mech. **224**, 91 (1991).
[28]B. Ran and J. Katz, ''Pressure fluctuations and their effect of cavitation inception within water jets,'' J. Fluid Mech. **262**, 223 (1994).
[29]G. A. Voth, K. Satyanarayan, and E. Bodenschatz, ''Lagrangian acceleration measurements at large Reynolds numbers,'' Phys. Fluids **10**, 2268 (1998).
[30]R. E. A. Arndt and W. K. George, ''Pressure fields and cavitation in turbulent shear flows,'' 12th Symposium on Naval Hydrodynamics, pp. 327–339.